



Time-Resolved Electrochemical Heat Flow Calorimetry for the Analysis of Highly Dynamic Processes in Lithium-Ion Batteries

Alexander Kunz,^{1,✉} Clara Berg,^{2,*} Franziska Friedrich,^{2,*} Hubert A. Gasteiger,^{2,**} and Andreas Jossen¹

¹Technical University of Munich, School of Engineering and Design, Department of Energy and Process Engineering, Chair of Electrical Energy Storage Technology; Arcisstraße 21, 80333 Munich, Germany

²Technical University of Munich, Department of Chemistry and Catalysis Research Center, Chair of Technical Electrochemistry; Lichtenbergstraße 4, 85748 Garching, Germany

Isothermal microcalorimetry is used to study the heat flow of lithium-ion cells to provide insight into active material characteristics and to provide data required for a thermal optimization on the cell and system level. Recent research has shown the application of this technique to cells during high cycling rates, for example fast charging. However, the limitation of isothermal microcalorimetry is the low-pass characteristic of the measured heat flow, introduced by the thermal inertia of the setup and the calorimeter itself. To solve this problem, we introduce an optimized cell holder design and a novel data processing method for a time-resolved measurement of highly dynamic heat flow profiles. These are described in detail and validated using a synthetic power profile applied to a dummy cell. Experiments on a graphite-lithium half-cell illustrate the improvement of the method and the optimized cell holder when compared to the state-of-the-art setup, demonstrating the 3.6 times faster time response, which was further improved using a post-processing deconvolution technique. The thus improved time resolution provides the acquisition of more detailed features than currently shown in the literature and allows an accurate correlation of the thermal signals to electrochemical features like, e.g., the differential voltage of the cell.

© 2022 The Author(s). Published on behalf of The Electrochemical Society by IOP Publishing Limited. This is an open access article distributed under the terms of the Creative Commons Attribution 4.0 License ([CC BY](http://creativecommons.org/licenses/by/4.0/), <http://creativecommons.org/licenses/by/4.0/>), which permits unrestricted reuse of the work in any medium, provided the original work is properly cited. [DOI: [10.1149/1945-7111/ac8625](https://doi.org/10.1149/1945-7111/ac8625)]



Manuscript submitted June 2, 2022; revised manuscript received July 13, 2022. Published August 16, 2022.

To increase the attractiveness of electric vehicles, the energy and power density of lithium-ion batteries (LIBs) need to be improved whilst maintaining good cycle life and safety. The performance of LIBs strongly depends on the operating temperature.¹ At low temperatures, the internal resistances become very high, which limits the driving range, driving performance (e.g., acceleration), and fast charging capability. At high temperatures, parasitic processes are enhanced, resulting in faster aging and an increased safety risk of batteries. The cell temperature is not only determined by the environment, but is greatly affected by the internal heat generated by the battery itself during charge and discharge.² To meet the current requirements for LIBs, research focus has shifted towards high-energy-density active materials. Lithium- and manganese-rich NCMs (LMR-NCMs) are examples of such cathode active materials with a superior energy density compared to conventional NCMs. However, their large voltage hysteresis between charge and discharge, even under open circuit voltage (OCV) conditions, results in a reduced energy efficiency during operation and in an increased heat evolution compared to conventional NCM or NCA cathode active materials.^{3–6} As a result, the study of heat generation in these active materials is important for the optimization of operating conditions and for the prediction of the cell and battery temperature during operation. Electrochemical calorimetry can be used in combination with electrochemical characterization methods such as impedance spectroscopy, incremental OCV cycling, and entropy measurements to distinguish between different sources of heat generation.^{7–9} This enables a better understanding of the impact of parasitic processes and their dependencies on factors such as the electrolyte composition,^{10–16} operating voltage,¹² and active material particle morphologies.¹⁷

The isothermal microcalorimeter TAM III/IV (TA Instruments/Waters) can be modified to study the heat generation of lithium-ion coin cells under isothermal conditions with high accuracy and has been widely used in reported studies.^{10–19} This setup was described

in detail by Krause et al.¹⁷ and is considered the state-of-the-art setup for electrochemical calorimetry on coin cells. Subsequent publications continued to use this setup,^{10–14,18,19} and since then no further modifications on the overall setup and particularly on the cell holder have been reported. Common to all these studies is the analysis of the generated energy by integrating the heat flow over time. However, features within the heat flow curve are also of interest for the detection and investigation of electrochemical processes. For the latter, the time-resolution of the signal is a major challenge, which is especially pronounced for the analysis of dynamic processes at increased C-rates. However, due to the thermal inertia of the setup, highly dynamic heat flow features may be attenuated or lost, so that the heat flow measured at faster C-rates cannot be clearly assigned to a particular state of charge (SOC), which makes the correlation of thermal data with electrochemical data difficult.

In this work, we present an optimized methodology for time-resolved electrochemical calorimetry using a modified cell holder design. An optimized new coin cell holder is described, which enables significantly better heat flow dynamics compared to the sample holder used in the literature. The measurement accuracy and time resolution of the new cell holder are characterized and compared to the currently used cell holder setup. Furthermore, the detailed description of the dynamic response to an electrical power signal applied to a dummy cell enabled the implementation of a dynamic correction method based on a computational deconvolution method, which allows to correct the recorded thermal signal for its time delay due to thermal inertia. This was illustrated for the lithiation of graphite with both the conventional and the here designed cell holder. A correlation between the first derivative of the graphite/lithium half-cell potential and the highly dynamic heat flow signal demonstrates the benefits of the new calorimeter cell holder design in combination with the dynamic correction method.

Cell Holder Optimization

The working principle of the TAM heat-conduction calorimeter is based on the measurement of a temperature difference $\Delta T(t)$ between the sample temperature T_{cal} and the temperature of the isothermal calorimeter environment (oil bath) T_{oil} . The heat $Q(t)$

^{*}Equal Contribution.

[†]Electrochemical Society Student Member.

^{**}Electrochemical Society Fellow.

[✉]E-mail: alexander.kunz@tum.de; clara.berg@tum.de

emitted or absorbed from the sample can be determined as a function of time, if the effective heat capacity of the setup C_{cal} is known:

$$Q(t) = C_{\text{cal}} * \Delta T(t) \quad [1]$$

The heat flow \dot{Q} corresponds to the derivative of this function. The time resolution of the measurement is determined by the heat exchange dynamics within the materials and the geometry of the calorimeter setup. In the currently used setup, the cell is freely hanging inside a stainless steel ampule as shown in Figs. 1 and 2a. This means that the heat generated from the cell needs to increase the temperature of roughly 20 cm^3 of air volume inside the ampule plus the 80 g of stainless steel of the ampule body before it is detected by the thermopile. Aiming to improve the heat flow dynamics, a new cell holder was developed for coin cell measurements as a replacement of the currently used ampule. Similar to the ampule, it holds the cell in the calorimeter and connects it to the sample lifter via a mounting, as schematically illustrated in Fig. 1. To electrically connect the cell holder, a 4-wire configuration was implemented which is described in detail below. Instead of using a Torr Seal® epoxy resin (Kurt J. Lesker Company) to cover the holes made for the wiring, a regular playdough (Pelikan Nakiplast®) allowed for an easier handling whilst providing the same thermal isolation and signal stability.

The new cell holder was optimized by minimizing the heat capacity of the components surrounding the heat source (cell), while increasing the thermal connection of the cell to the thermopile. To characterize the thermal connectivity, the figure-of-merit is the thermal diffusivity D_t , which is the ratio of the material's heat conductivity $\lambda (\text{W m}^{-1} \text{ K}^{-1})$ to the specific heat capacity $c_p (\text{J kg}^{-1} \text{ K}^{-1})$ multiplied by the density $\rho (\text{kg m}^{-3})$:

$$D_t = \frac{\lambda}{\rho c_p} \quad [2]$$

The multiplication with the density transforms the mass-normalized heat capacity to a volume-normalized property, which is suitable for the comparison of different materials for the same cell holder geometry. Table I displays literature data of silver, gold, and copper which are the metals with the most suitable thermal properties. They offer thermal diffusivities that are orders of magnitude higher compared to the stainless steel that is used for the conventional ampule sample holder. Even though silver and gold exhibit the highest thermal diffusivities, copper was found the most suitable material due to its hardness and the resulting easier machinability. Copper undergoes some surface corrosion when exposed to air due to ongoing oxidation; thus, the new cell holder was coated with a thin ($<1 \mu\text{m}$) layer of gold via an electroplating process.

Figures 2a and 2b show the ampule sample holder and optimized new cell holder, respectively. In contrast to the vertical coin cell orientation in the ampule, the cell is positioned horizontally in the new cell holder. This minimizes the distance between the cell and the thermopile. In addition, the positioning of the cell is tightly controlled and reproducible, whereas for the ampule the cell is oriented at a different angle depending on the rotation at which the ampule is inserted. The height at which the cell is positioned inside the calorimeter was optimized by modifying the length of the mounting to place the cell as close as possible to the thermopile. This mounting was made from a glass fiber material with poor thermal conductivity in order to minimize heat exchange into that direction.

For the optimization of the cell holder geometry, thermal simulations (3D COMSOL Multiphysics Version 5.6) were performed. Figure 2c shows the heat flow simulation for the ampule that was used in previous publications,^{11–14,17–19} and Fig. 2d shows the heat flow simulations of the geometry of the new cell holder. Here, the focus was on determining the transient temperature distribution of the two setups by implementing a coin cell model that dissipates a

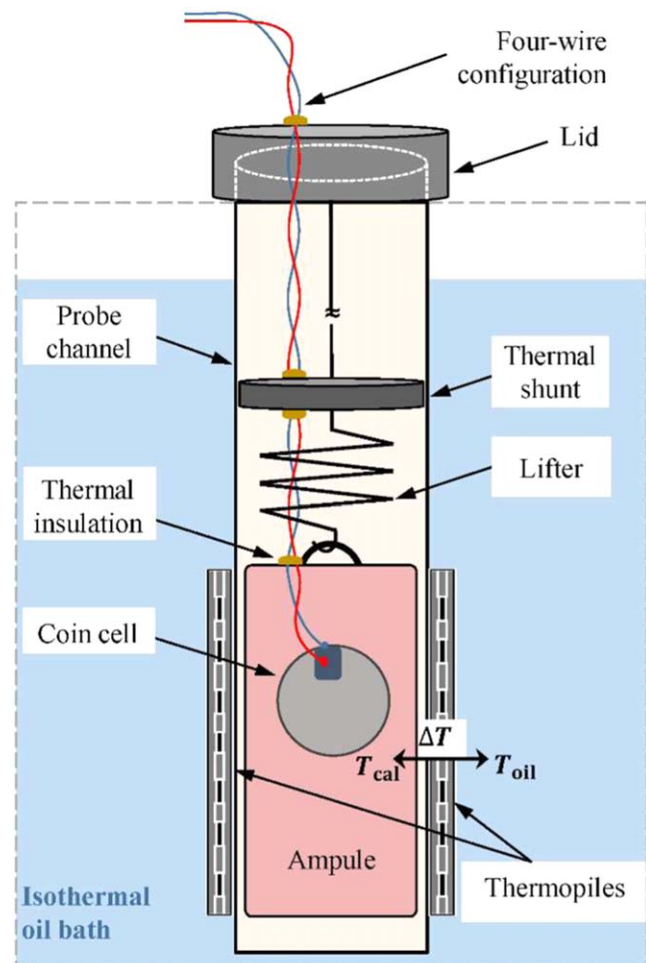


Figure 1. Schematic of the state-of-the-art setup for electrochemical calorimetry on coin cells using the TAM IV microcalorimeter. An oil based liquid bath controlled by a thermostat enables the quasi-isothermal measurement environment around the cylindrical probe channel. Within the channel, the cell is inserted into the stainless steel ampule, which is hanging on the lifter.

constant thermal power of 1 mW. The temperature difference ΔT with respect to the initial temperature is shown after a simulation runtime of 200 s. It can be seen that the air in the ampule is isolating the cell from its surrounding, so that the heat flow causes a temperature increase of the cell itself in comparison to its local ambience: the major part of the emitted heat is transferred via the electrical wires away from the thermopiles rather than being transferred directly to the ampule housing via heat conduction through the air. In contrast to that, the thermal model for the new cell holder indicates that there is no temperature gradient between the cell and the outer walls of the cell holder after 200 s, thus fulfilling the requirement for isothermal calorimetry. The poor thermal conductivity of the glass fiber mounting is indicated by the high color gradient along the vertical direction.

It can be seen that with the new cell holder, a part of the heat is also dissipated via the wires as heat leak (see Fig. 2d). This heat loss would decrease with thinner wires, which on the other hand would lead to a higher self-heating due to a higher ohmic resistance of thinner wires, particularly at cell higher currents. Therefore, an optimum was found to minimize both of these unwanted effects by choosing a wire cross section of 0.0503 mm^2 (30 AWG) for a wire length of approximately 12 cm starting at the cell contact. Outside the measuring region of the calorimeter, the force-wires which carry the current were replaced by cryogenic phosphor bronze wires with a cross section of 0.0123 mm^2 (36 AWG), which act as a barrier against parasitic influences because of their lower thermal conductivity. The

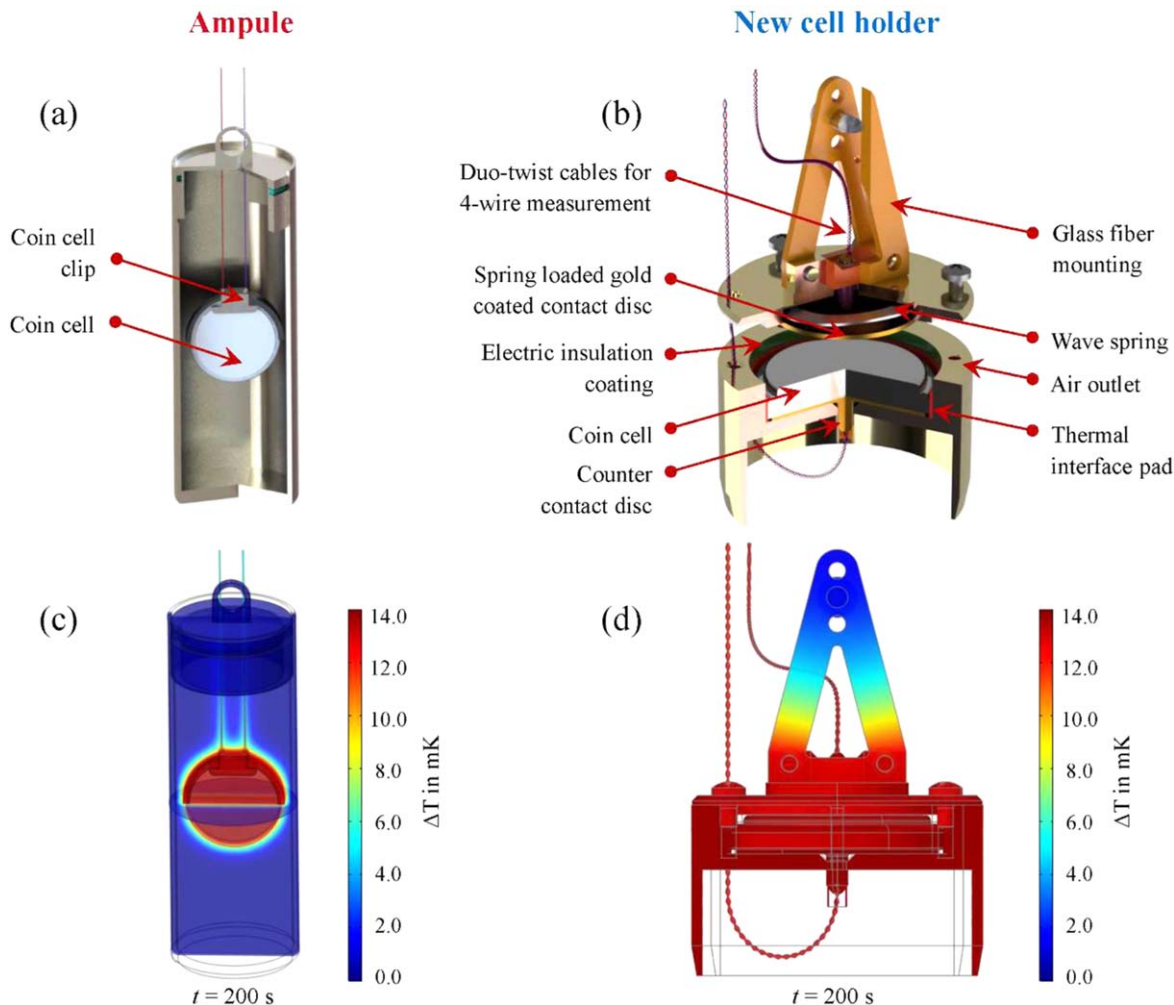


Figure 2. Illustration of the stainless-steel ampule (a) and the new cell holder (b) for calorimetry measurements on coin cells. The lower panels show the temperature increase of the initially isothermal cell holders after applying 200 s of a constant heat flow (1 mW) to the of the ampule (c) and the new cell holder (d), as determined by a thermal transient simulation in COMSOL.

sense-wires for the cell voltage measurement are made completely with the cryogenic phosphor bronze wires with a cross section of 0.0123 mm^2 (36 AWG), because there is no effect of self-heating in the absence of current flow which allows to use these high resistance wires to minimize the heat loss from the cell holder. The simulation results reveal that the proportion of heat flow leaking via the wires could be reduced from up to 38% (ampule) to less than 1% with the new cell holder, increasing the sensitivity of the heat flow measurement.

Another optimization was made in regards to the air gap between the ampule and the calorimeter. In contrast to the ampule, the diameter of the new cell holder is larger, resulting in less space between the calorimeter wall and the cell holder, thereby minimizing the thermal resistance of this air gap (0.01 mm for the new design vs 0.08 mm for the ampule design). To further minimize this thermal resistance, the height of the cell holder wall was optimized by considering the trade-off between maximal surface area for this heat transfer to the calorimeter and minimal thermal mass by the thermal simulation. Finally, in order to simplify the insertion and extraction of the sample into the calorimeter shaft without wedging and getting stuck, there is a 20° -chamfer on the bottom part and a 35° -chamfer on the top part of the new cell holder. Next to the holes for the screws and for the wiring, there is an additional hole to allow the passage of air in order to avoid the build-up of pressure during insertion of the cell holder.

The edges of the cell holder are covered with a flexible and compressible silicon thermal interface pad (MPGCS-040-150-0.5,

multicomp-pro, with $\lambda = 4.0 \text{ W m}^{-1} \text{ K}^{-1}$ and a thickness of 0.5 mm) to maximize the contact surface to the edges of the coin cell. All cell holder parts which are in contact with the cell but must be electrically insulated from each other are covered with an electrically insulating coating (CRC PLASTIC 70, with a thickness of $\sim 40 \mu\text{m}$ and a surface resistivity of $> 10^{13} \Omega$ at 20°C). The coin cell was electrically contacted via flat, gold-coated contact surfaces on the top and the bottom part of the cell holder. To ensure good contacting of the coin cell, the top contact of the cell holder is spring-loaded with a pressure of about 1.5 bar. The initial idea to use spring-loaded gold contact pins was rejected, as they exhibited a small but unstable contact resistance that resulted in an unstable parasitic heat contribution to the measured signal. For the investigation of half-cells, we recommend to place the working electrode directly at the can of the coin cell, since this part is placed at the bottom of the cell holder and is thus thermally best connected (for the suggested cell assembly, see Fig. 3b below).

Characterization of Measurement Accuracy and Time Resolution

Accuracy of the heat flow measurements.—As described above, the effective heat capacity C_{cal} of the involved experimental setup (sum of cell, cell holder, wiring, calorimeter components, etc) needs to be determined for a calculation of the thermal power (i.e., heat flow) from the measured temperature difference. To do this, a so-called gain calibration is performed prior to each measurement. This

Table I. Comparison of thermal material properties and range of values for pure metals at 20 °C. The cell holder was made from the Cu alloy stated in parentheses. Values for the density, the specific heat capacity and the thermal conductivity were collected from material handbooks^{20,21} to enable a qualitative comparison of various metals in terms of thermal diffusivity. The stated thermal diffusivities were calculated using Eq. 2.

Material	Density ρ [g cm ⁻³] ²¹	Specific heat capacity c_p [J g ⁻¹ K ⁻¹] ²⁰	Thermal conductivity λ [W cm ⁻¹ K ⁻¹] ²¹	Thermal diffusivity D_t [cm ² s ⁻¹]
Silver	10.50	0.235–0.239	4.28	1.71–1.73
Gold	19.28	0.126–0.130	3.18	1.27–1.31
Copper (ETP Cu)	8.93 (8.89)	0.387–0.393 (0.385)	4.01 (3.91)	1.14–1.16 (1.14)
Stainless steel	7.50–8.25	0.460–0.586	0.312	0.065–0.090

	(a) Dummy Cell	(b) Graphite/Lithium Cell	(c) Calibration Cell
Cell Cap			
Gasket			
Wave Spring			
Spacer			
Lithium Foil			
2x Glass Fiber Separator			100 Ω High-Precision Calibration Resistor
Coating on Copper Foil	Charcoal Coating (facing down)	Graphite Coating (facing up)	
Cell Can			

Figure 3. Overview of the test cells used in this publication: (a) charcoal dummy cell, (b) graphite/lithium half-cell, and, (c) calibration cell. The dummy cell was developed to match the half-cell in regards to its thermal properties. 2032 coin cell parts were used for all cell types. The stainless steel spacers had a thickness of 1 mm. The lithium-foil (450 μm thickness, 99.9%, Rockwood Lithium) and the charcoal and graphite coatings were punched with a diameter of 15 mm. The areal loadings of the charcoal and graphite coatings were 3.36 mg cm^{-2} and 5.07 mg cm^{-2} , respectively. The glass fiber separators (VWR) had a diameter of 17 mm. For the dummy cell, the separators were cut and a narrow strip of copper foil was inserted to electrically connect the lithium foil to the charcoal coating via the copper foil. The separators were soaked in 100 μl silicone oil and 80 μl LP57 electrolyte for the dummy and graphite/lithium cells, respectively. Details on the preparation of the graphite electrodes are given in Section IV.

can be done internally or externally. For an internal calibration, a known thermal power is applied via a built-in heat source located next to the heat flow sensor. For an external calibration, the thermal power is applied by a heat source in the probe volume of the calorimeter (e.g., a resistor in the ampule). The second procedure was reported by Krause et al.,¹⁷ where the gain was determined by applying 50 μW electrical power to a calibration coin cell comprising of a precision resistor, which is placed hanging inside of the ampule. In the first experiments, we compared these methods to determine the gain. From the results (not shown here), we concluded that a higher accuracy can be obtained with the external gain calibration method. Typically, a gain in the range of 1.01–1.04 was obtained for both setups.

The external gain calibration method was used for all subsequent measurements in our study, using an in-house built calibration cell made from a 100 Ω precision resistor (Z201, Z Foil from VISHAY Precision Group) embedded into a coin cell casing. Figure 3c illustrates the main components of this calibration cell. The used resistor exhibited a low temperature coefficient of resistance (TCR) of $\pm 0.2 \text{ ppm } ^\circ\text{C}^{-1}$, ensuring a constant thermal power dissipation during the calibration procedure. This resistance value was chosen in order to align the current that is necessary for a given heat flow dissipated by a graphite/lithium coin cell (determined in preceding experiments) and the current applied to the calibration cell. By doing so, the accuracy obtained from the calibration process with the calibration cell can be assumed to be valid for a real coin cell experiment, since the impact of the parasitic heat arising from wire or contact resistances (only dependent upon the current) is identical and since the same range of heat evolution rates were chosen. The electrical connection inside of the calibration cell was made by welding a nickel-plated steel chip (HILUMIN®, Tata Steel, thickness

0.2 mm) with a size of 4 by 4 mm onto the stainless steel cell case. The chip was used, since it is not possible to solder directly onto the stainless steel cell case. One resistor pin was directly soldered onto the chip, the other pin was soldered first to a wire with a cross section of 0.0503 mm^2 (30 AWG), which was then soldered onto the chip on the other side of the cell casing. For proper thermal connection of the resistor to the cell casing, a thermal paste (WLPK10, Fischer Elektronik, with $\lambda = 10 \text{ W m}^{-1} \text{ K}^{-1}$) was used together with a thermal glue (TC2707, 3 M).

After the external gain calibration conducted at 50 μW , we evaluated the accuracy at steady-state for different applied powers in the range of 50–300 μW . For this purpose, we reinserted our calibration cell into the new cell holder, as we would insert a real cell. Using the same potentiostat as used for the calibration and all experiments described in the following (VSP-300, BioLogic Science Instruments), electrical power steps in the range of 50–300 μW for two hours each were applied. We assumed that the heat flow would settle at a constant power in less than one hour. Therefore, we averaged the applied and measured power during the second hour of each pulse. Table II shows the measured heat flow versus the applied electrical power. The relative error of the detected steady-state heat flow was smaller than $\pm 0.05\%$ in the investigated thermal power range. The same maximum deviation was found for several repetitions of the experiment indicating high accuracy and reproducibility of the setup.

Time resolution of the heat flow signals.—In the following, the time resolution of a measurement in the new cell holder was characterized and compared to the ampule setup by applying artificial electrical power step signals. To include the thermal inertia of an actual test cell, we developed a dummy cell that has nearly

Table II. Measured thermal power versus applied electrical power using the calibration cell (see Fig. 3c) at 25 °C, displaying the accuracy of the optimized new cell holder setup after an external calibration for applied powers in the range 50 μW–300 μW.

Applied power [μW]	Measured power \dot{Q}_{cal} [μW]	Difference [μW]	Fractional difference
50.10	50.12	0.02	1.0004
100.25	100.24	-0.01	0.9999
150.30	150.32	0.02	1.0001
200.70	200.80	0.1	1.0005
251.00	251.02	0.02	1.0001
301.00	300.98	-0.02	0.9999

identical thermal properties compared to a lithium-ion half-cell but that does not exhibit any electrochemical processes. For this, we adapted the coin cell setup, using most of its components but replacing the working electrode by a high-resistance charcoal coating on a copper foil. Figures 3a and 3b schematically illustrate the dummy cell and the graphite/lithium half-cell setup, respectively. The dummy cell coating was made from a slurry containing 87%_{wt} of finely ground charcoal (Natural Charcoal Stick, Faber-Castel) and 13%_{wt} of sodium carboxymethyl cellulose (CMC, MAC200HC, SUNROSE) dispersed in water. Furthermore, the separators were soaked with 100 μl of silicone oil instead of electrolyte. The charcoal coating was electrically connected to the lithium counter electrode by a narrow strip of copper foil fitted through a slit in the glass fiber separators. The final dummy cell exhibited an electrical resistance of approximately 35 Ω, thus, heat can be produced upon application of a current. It is expected that most of the heat is produced on the full area of the charcoal electrode. In order to verify a comparability of this charcoal dummy cell to an actual graphite/lithium half-cell, the heat measured for a change in thermostat temperature of the TAM IV due to the thermal mass of the respective cell was compared.

For this purpose, the oil bath temperature was increased from 25 °C to 27 °C, with the dummy or the graphite/lithium cell in the cell holder inside the sample channel and with an empty cell holder in the reference channel. The resulting measured heat flow was integrated over 6 hours to obtain the full energy required for heating the cell by 2 K. Dividing this energy by 2 K yielded a thermal mass in units of J K⁻¹. This method was validated by the use of an aluminum disk (Al99.5, with 20 mm diameter, 3.2 mm height) with a known specific heat capacity of 901 J kg⁻¹ K⁻¹). According to the measured weight of 2.734 g, we expected a thermal mass of 2.45 J K⁻¹. We measured a value of 2.42 J K⁻¹, indicating a relative error/uncertainty of ~1.2%. For both the charcoal dummy cell and the graphite/lithium half-cell described in Section IV, an essentially identical thermal mass of 2.2 J K⁻¹ was measured. Thus, the charcoal dummy cell is suitable for the characterization of the time-delay of the heat signal response that is representative of what would be expected for a graphite/lithium half-cell.

The dynamics of both the optimized new cell holder and the ampule were characterized using this dummy cell. For the conventionally used setup, the dummy cell was placed hanging inside the ampule, fixed with a commercial plastic cell clip as depicted in Fig. 2a; alternatively, the dummy cell was placed into the new cell holder. We then conducted heat flow pulse experiments, using constant power settings in the range of 10–1000 μW, whereby a given electrical power P_{el} was applied to the dummy cell for 2 h, with 6 h of relaxation period before the next pulse at a different power setting. Once the electrical power was applied, we analyzed the transient heat flow until the heat flow reached a steady-state. The heat flows for each power setting, normalized by the respective steady-state heat flow value versus time are shown in Fig. 4 for both the ampule (red) and the new cell holder (blue). By doing so, we received the unit step response of the calorimeter by comparing the electrical power applied to the calibration cell (= input signal) to the

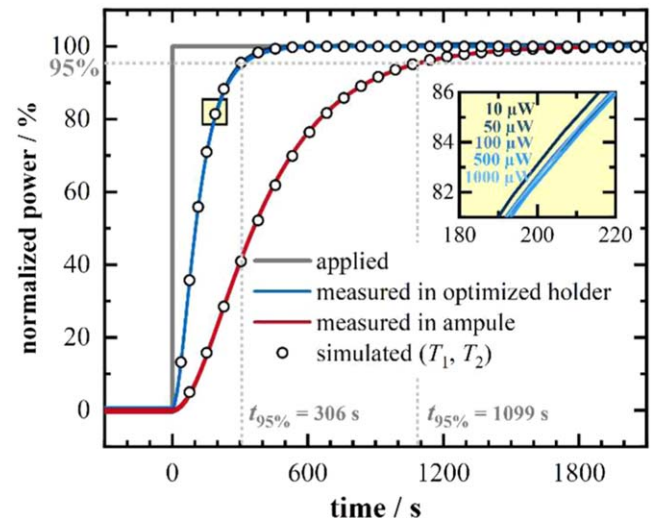


Figure 4. Comparison of the measured transient heat flow normalized by the steady-state heat flow for the setup using the ampule (red) and the optimized new cell holder (blue). Constant electrical power steps (gray) were obtained by applying a constant current for two hours each to the charcoal dummy cell (see Fig. 3a). The step response can be described as a PT2-system with the time-constants T_1 and T_2 that can be determined by a fit of Eq. 3 (circular markers).

measured heat flow signal (= system output). As can be seen in Fig. 4, the dynamic behavior of the ampule and the new cell holder is independent from the applied power (between 10–1000 μW), since all 6 normalized power steps are superimposed and appear as one line (see inset in Fig. 4). However, a comparison of the measured heat flow between the new cell holder and the ampule shows that the heat flow measured with the new cell holder rises significantly faster. The left-most columns of Table III list the time durations until specific percentages of the applied signal amplitude (90, 95, and 99%) were reached for the two different setups, clearly showing that the heat flow signal of the new cell holder settles at its steady-state approximately 3.6 times faster than that of the ampule.

By analyzing the heat flow step response of the calorimeter, an inflection point is seen in Fig. 4 for both setups, suggesting that the response is associated to a second-order system.²² More precisely, the response of the system to the unit step input does not exhibit any overshoot or oscillating parts in the measured heat flow \dot{Q}_{cal} for both setups. Therefore, the damping factor ζ , is greater than or equal to 1, corresponding to an overdamped second order system. In general, to express the dynamics of a second-order system, in conjunction to ζ , the natural frequency ω_0 is defined as the frequency with which the system would oscillate if it were not damped enough. However, in our case the dynamics of the calorimetric setup can be described solely by two time constants. The output of the calorimeter system $\dot{Q}_{\text{cal_step}}$ to an applied step function P_{el} can be described by the

Table III. Parameters describing the heat flow time response of the ampule and new cell holder setup determined for a constant electrical power applied to the dummy cell (see Fig. 3a). The displayed parameters correspond to the average of the values obtained for each of the applied power steps between 10 and 1000 μW . Column 1–3 state the duration until a certain percentage of the final heat flow value corresponding to the applied electrical power is reached. The time constants T_1 and T_2 describe the second order low-pass behavior of the calorimeter. The thermal mass C_p corresponds to the energy needed to increase the temperature of each setup by 1 K. For each parameter, the ratio ampule / new cell holder is displayed in the bottom row.

	90% /s	95% /s	99% /s	T_1 /s	T_2 /s	$T_1 + T_2$ /s	C_p /J K $^{-1}$
Ampule	895.1	1098.9	1561.2	169.28	270.14	439.42	41.54
New cell holder	249.3	306.2	434.0	47.93	74.91	122.84	11.94
ratio	3.60	3.59	3.60	3.53	3.61	3.58	3.48

following equation as a function of time t :

$$\dot{Q}_{\text{cal_step}} = K \cdot \left(1 - \frac{T_1}{T_1 - T_2} e^{-\frac{t}{T_1}} - \frac{T_2}{T_2 - T_1} e^{-\frac{t}{T_2}} \right) \cdot P_{\text{el}} \quad [3]$$

where K is the amplification factor, P_{el} the applied electrical power, and T_1 and T_2 are the time constants describing the dynamics of the system. As an external calibration had been performed prior to the measurement (see previous subsection), the amplification factor K was set to 1. From our evaluation of the accuracy of the measurement at different applied powers (Table II), we expect K to have a maximum error of 0.05%. For the system identification purpose, the time constants T_1 and T_2 were found by using the nonlinear least-squares solver (*lsqcurvefit*) function in MATLAB. The following equation was used in this implementation:

$$\begin{aligned} & \min_{T_1, T_2} \|F(T_1, T_2, xdata) - ydata\|_2^2 \\ &= \min_{T_1, T_2} \sum_i (F(T_1, T_2, xdata_i) - ydata_i)^2 \end{aligned} \quad [4]$$

where the nonlinear function F is Eq. 3 and serves as a model for the measured calorimetric data $ydata$. The measured time data or t is represented by $xdata$. The initial guess for the algorithm was $T_1 = 50$ s and $T_2 = 90$ s after visual inspection of the measured calorimetric data. To accelerate the solving process, a lower and upper boundary for both coefficients was defined as 0 s and 1000 s, respectively. The stop criterion for the iteration of the fitting algorithm was set to when the change of the relative sum of squares was smaller than 10^{-7} per iteration. The fitting was completed after seven iterations and the quality of the fitted data was compared to the measured data. The accuracy of the fit was evaluated by calculating the root mean squared error (RMSE), which is the standard deviation of the residuals and indicates how concentrated the measured data is around the fitted curve. The calculated RMSE value was 0.0042. The average value between the different power steps was calculated for each of the two time-constants. The resulting values are displayed in Table III. The maximum deviation for the time-constants was smaller than ± 0.35 seconds between the different power steps. The step response according to Eq. 3 was plotted with the derived time-constants and is shown in Fig. 4 (circular markers).

We determined the thermal masses of the new cell holder and the ampule as 11.94 J K^{-1} and 41.54 J K^{-1} respectively, as done for the charcoal dummy. The heat capacity of the ampule was approximately 3.5 times higher than that of the new cell holder. This ratio matches the ratios of the different time constants displayed in Table III. Thus, we considered the ratio in heat capacity of the two setups as the major reason for the difference in dynamics. An overdamped second order system can be described by two first-order systems with one time constant each. However, we were not able to assign the constants to a specific dynamic process during the transient response. For example, by varying the thermal properties of the coin cell or of the cell holder material, we observed a change in both time constants, so that the time constants do not uniquely

represent the thermal mass of either component. In addition to the evaluation of the signal rise behavior shown in Fig. 4, we also analyzed the decay of the heat flow after the electrical power was turned off (data not shown), observing no difference in the transient behavior. In addition to the faster dynamics of the new cell holder, another benefit compared to the ampule is that the thermal equilibrium is reached more quickly after inserting a new cell into the calorimeter, resulting in a shorter preparation time until a new measurement can be started.

Dynamic Correction of Measured Signals

Computational deconvolution method.—In Section II, it was described how the time resolution of the heat flow signal can be improved by a hardware optimization in the measurement setup. For further improvement of the signal in terms of edge sharpness, we used the technique of deconvolution to post-process the measured heat flow signal. Using the known dynamic system characteristics, the goal was to deconvolute or separate the heat flow contribution originally arising from electrochemical cell reactions from the inherent contribution of the setup to the heat flow signal, caused, for instance, by the cell casing, the cell holder, or the calorimeter instrument itself. The concept of convolution can be described by the following equation:

$$g(x) = f(x) * h(x) + n(x) \quad [5]$$

where $g(x)$ is the heat flow signal measured by the calorimeter, $f(x)$ is the heat flow from the electrochemical process in the cell, $h(x)$ is the system function introduced by the calorimeter and convolved (*) with the heat flow, and $n(x)$ is the noise in the system. For special use cases such as solving multi-dimensional transformations or recovering signals from highly distorted convolutions, there is a variety of algorithms for deconvolution. For example, the Wiener deconvolution algorithm can be applied to recover an input signal from an output signal that is severely corrupted with noise. In this work, we employed the simplest form of deconvolution, the inverse filter, which ignores the potential impact of noise $n(x)$ and excludes denoising techniques. The deconvolution is simply a division in the frequency domain between the measured heat flow signal and the system function of the calorimeter. This approach was chosen due to the well-posed nature of the deconvolution problem for the measured heat flow signal, i.e., the known impulse response of the system $h(x)$ as discussed below, and the high signal to noise ratio (SNR) of the measurement data, which is greater than 60 dB in the signal power spectrum.

Using the previously determined time constants, the step response $g(t)$ was simulated by measuring the heat flow of the dummy cell and is shown in Fig. 4. The impulse response $h(t)$ resulted from the derivative of the step response with respect to time. Assuming the same setup for all subsequent experiments, this impulse response calculation was performed once for each of the two setups in advance of the experiment with the graphite/lithium half-cells. This signal path is indicated with dashed arrows in Fig. 5. In contrast, the graphite/lithium half-cell heat flow signal processing path is displayed with the solid arrows. Here, the measured heat flow $y(t)$

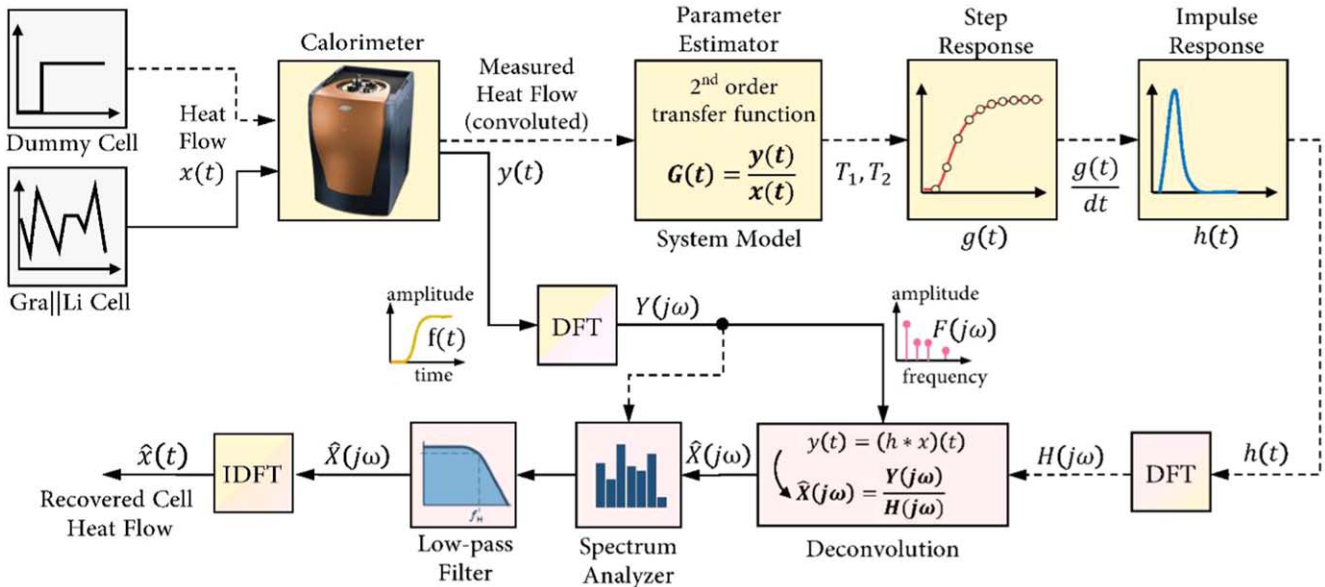


Figure 5. Schematic illustration of the heat flow recovery method. Prior to the experiment with a real coin cell, the setup characterization process occurred, indicated by the dashed arrows. During the characterization process, the heat flow response was measured by applying a constant power to the charcoal dummy cell. The measured step response was converted to an impulse response and transferred to the frequency domain by a discrete Fourier transform (DFT). To recover the signal from a real coin cell, the measured signal from the real coin cell was first transferred to the frequency domain by a DFT. Then this measured signal was deconvoluted from the system impulse response determined by the characterization process, i.e., by division in the frequency domain. To restore the original frequency spectrum, a low-pass filter was applied. The recovered heat flow in the time domain was received by an inverse discrete Fourier transform (IDFT).

(previously referred to as \dot{Q}_{cal}) was transferred into the frequency domain by a discrete Fourier transform (DFT) and is shown as $Y(j\omega)$. The impulse response was also converted by a DFT into the frequency spectrum $H(j\omega)$.

The inverse filter deconvolution was then performed by a division in the frequency domain, $Y(j\omega)/H(j\omega)$. Even though there is only a small amount of noise in the measured data, it is still common that high-frequency components are disproportionately amplified during the deconvolution. In order to reduce the additional noise and ringing in the recovered signal, we analyzed and compared the power spectrum of $Y(j\omega)$ and $\hat{X}(j\omega)$. The observed high-frequency components in the spectrum of the recovered signal $\hat{X}(j\omega)$ that were introduced by the deconvolution process were rejected with a standard Finite Impulse Response (FIR) low-pass filter implemented in the MATLAB Signal Analyzer Toolbox. The retained low frequency components were assigned to the actual measured signal from the real cell. The filter was at first applied directly to the measured signal and compared with the unfiltered measured signal. This ensured that any frequency components in the spectrum before the deconvolution were not changed, such as an introduced constant filter delay. This was proven by calculating the Pearson correlation coefficient between the measured signal and the measured signal with the directly applied low-pass filter. Subsequently, the inverse discrete Fourier transformation (IDFT) of $\hat{X}(j\omega)$ was performed, and $\hat{x}(t)$ was interpreted as the best-estimated original heat flow from the electrochemical reaction and is denoted in the following as “recovered” heat flow.

The toolchain of the new method was validated by using the dummy cell for recording the heat flow step response for both the new cell holder as well as the ampule setup. During the validation, the real cell heat flow was imitated by a synthetically generated and defined thermal power profile released from the dummy cell, with the goal being to recover this power profile. The applied power profile is displayed in Fig. 6 in gray. The synthetically created data was used, since we wanted to directly compare the released cell heat flow to both the measured heat flow and to the recovered heat flow after the recovery process.

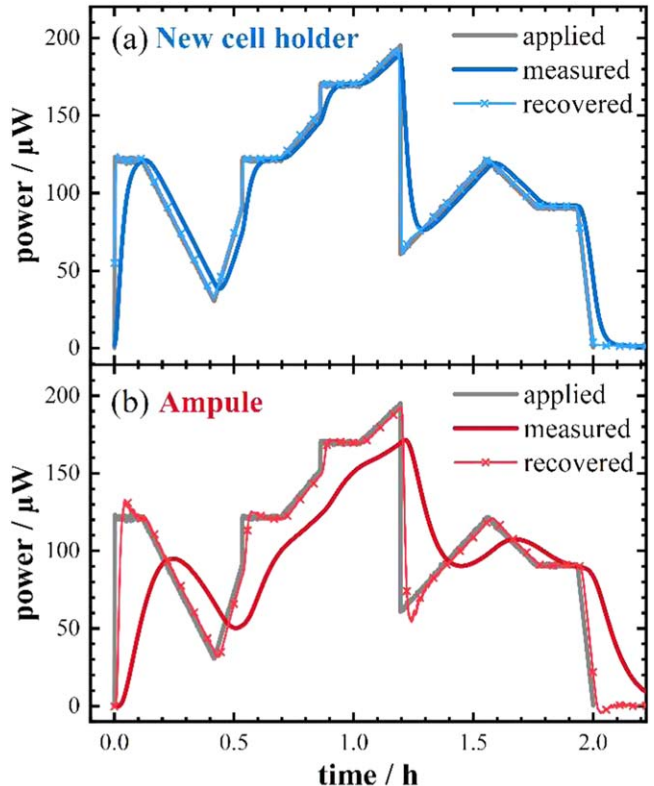


Figure 6. Applied, measured, and recovered dynamic power profiles for the new cell holder (a) and the ampule (b). The arbitrary synthetic electrical power profile was obtained by applying a current profile to the charcoal dummy cell (see Fig. 3a).

During the 2 h validation experiment with the dummy cell, we applied a power profile including a variety of variously shaped heat flow features with a duration in the range 4–20 min. The features were

used in order to observe the spectrum of the measured and deconvoluted heat flow. We considered the dynamic of heat flow features included in the validation profile to be in the range of the dynamics of the heat flow we would potentially be interested in obtaining later with a real coin cell. Based on the analyzed frequency spectra, the filter was tuned in a way that the estimated heat flow matched the frequency spectrum of the measured signal. The filter parameters resulting from that tuning were kept constant throughout this work and for both setups identical: stopband attenuation ($=20$ dB), steepness ($=0.95$), and passband frequency ($=0.5$ mHz) were used. Afterwards the estimated original heat flow was plotted for the optimized new cell holder and the ampule setup, as shown in Fig. 6. The effectiveness of the recovery process can be seen in Fig. 6, where the recovered signal measured with the optimized new cell holder has the highest correlation to the applied electrical power (gray line). In comparison to the ampule signal, it can also be seen that the deconvolution benefits from the hardware improvement, as the information loss is greater with the ampule setup, causing artefacts, such as overshoots for fast changes in the slope of the input signal.

Application to determine dynamic heat flows during graphite lithiation.—The lithiation of graphite has been studied extensively by means of calorimetry. In the literature, heat flow profiles have been reported with varying time resolutions.^{19,23} The lithiation of graphite displays distinct features in the heat flow which correspond to the different stages of lithium intercalation into the graphite layered structure. Due to the high dynamics of these features, especially at increased C-rates, we have considered this electrochemical process as a suitable showcase to illustrate the here suggested improvements in the time resolution of calorimetric heat flow measurements by both cell design and computational data post-processing.

Graphite electrodes consisting of 95.8%_{wt} graphite (SMG, BASF SE), 1%_{wt} carbon black (Super C65, TIMCAL), 1%_{wt} sodium carboxymethyl cellulose (CMC, MAC200HC, SUNROSE), and 2.2%_{wt} polystyrene-co-butadiene rubber (SBR, Sigma-Aldrich) were prepared with an areal capacity of 1.7 mAh cm^{-2} . Half-cells were prepared according to the schematic illustration in Fig. 3b. $80 \mu\text{l}$ of LP57 (1 M LiPF₆ in EC:EMC 3:7, BASF SE) were used as electrolyte. Each cell underwent ten formation cycles at C/10 constant current (CC) between the cutoff potentials of 10 mV and 1 V. Heat flow measurements were performed for different C-rates, whereby for each C-rate two cycles were performed and the lithiation of the second cycle was analyzed. Before and after the analyzed lithiation process in the second cycle, the cell was relaxed at OCV for 3 h to clearly separate the heat from the preceding and the subsequent delithiation. All measurements were performed with the thermostat of the calorimeter set to 25 °C.

Figure 7 depicts the as-measured heat flow data recorded during graphite lithiation in the graphite/lithium half-cell at C/10 for measurements performed with the new cell holder (blue line) and with the ampule (red line). The distinct features visible especially at the beginning of the lithiation (between 0 and $\approx 100 \text{ mAh g}_{\text{Gra}}^{-1}$) nicely correlate with the first derivative of the potential with respect to the capacity (dV/dQ , see gray lines in Fig. 7), suggesting that they correspond to changes in the electrochemical lithiation process of graphite. As was seen for the charcoal dummy cell experiments in the previous sections, a difference in the heat flow dynamics of the cell holders can be observed also for the graphite/lithium half-cells. Even though the heat flow signals for both setups trace out the same features, the signal recorded with the optimized new cell holder exhibits sharper edges and generally higher amplitudes (blue lines in Fig. 7). The small feature at $\sim 60 \text{ mAh g}_{\text{Gra}}^{-1}$ is only clearly distinguishable for the measurement with the new cell holder (best seen in the inset of Fig. 7). In addition, the features recorded in the ampule (red lines) are shifted in time and can therefore not be correlated as precisely to the dV/dQ profile. This is consistent with the above-determined better heat flow dynamics between the cell and

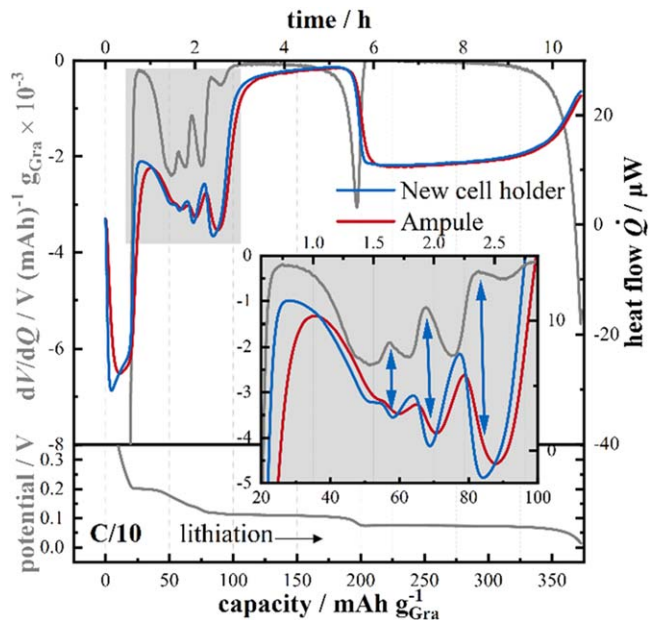


Figure 7. As-measured heat flow traces during the lithiation of graphite in a graphite/lithium coin cell using the optimized new cell holder (blue) and the ampule setup (red). The gray lines show the cell potential versus capacity (lower panel) and the derivative of the cell voltage with respect to capacity dV/dQ versus capacity (upper panel and inset). The blue arrows in the zoomed-in inset show the correlation of the dV/dQ features and the heat flow measured using the new cell holder. The graphite electrode has an areal capacity of 1.7 mAh cm^{-2} , and is cycled at C/10 at constant current between 10 mV and 1.0 V after 10 formation cycles ($80 \mu\text{l}$ of LP57 electrolyte and 2 glass fiber separators were used).

thermopiles of the calorimeter. As the region at the beginning of lithiation displays the most distinct features and is also accessible within the voltage limitations at higher C-rates, the following discussion focusses on the lithiation in the range of $0\text{--}220 \text{ mAh g}_{\text{Gra}}^{-1}$.

For measurements at higher C-rates, the improved dynamics of the new cell holder and the resulting higher resolution of heat flow features become more apparent. Figure 8a shows the recorded as-measured heat flow signals for C-rates between C/10 and 1 C (upper panel) and the lithiation potentials (lower panel) versus the specific lithiation capacity. The relatively low areal capacity loading (1.7 mAh cm^{-2}) enables a lithiation which is not significantly limited by transport resistances. Therefore, a parallel shift (rather than a smearing) of the lithiation voltage plateaus can be observed for the investigated C-rates, suggesting a mostly homogeneous lithiation across the graphite electrode thickness. Under this assumption, the lithiation features occurring at different C-rates should be similar and should result in similar features in the heat flow curves. This is indeed confirmed by the measurement with the new cell holder, especially in the range of C/10–C/4, where the heat flow features only change in magnitude. Comparing the heat flow traces obtained with the new cell holder (Fig. 8a) versus those obtained with the ampule setup (Fig. 8b), it becomes apparent that the heat flow features obtained with the former at C/4 are still better resolved than those obtained with the ampule at C/10. When comparing the endothermal feature at the beginning of lithiation between $0\text{--}30 \text{ mAh g}_{\text{Gra}}^{-1}$ and the small features between $30\text{--}100 \text{ mAh g}_{\text{Gra}}^{-1}$ in Figs. 8a and 8b, it can be seen that the amplitudes are significantly damped for the ampule setup. Especially at 1 C, the curve is much less defined and most of the features are not anymore discernible.

With increasing C-rate (i.e., with increasing current I), the magnitudes of the recorded features change as a result of the current dependency of the different heat sources in the graphite/lithium half-cell. The heat flow of the cell \dot{Q}_{cal} can be expressed as a sum of (i) polarization or irreversible heat \dot{Q}_{pol} , (ii) reversible heat \dot{Q}_{rev} , and

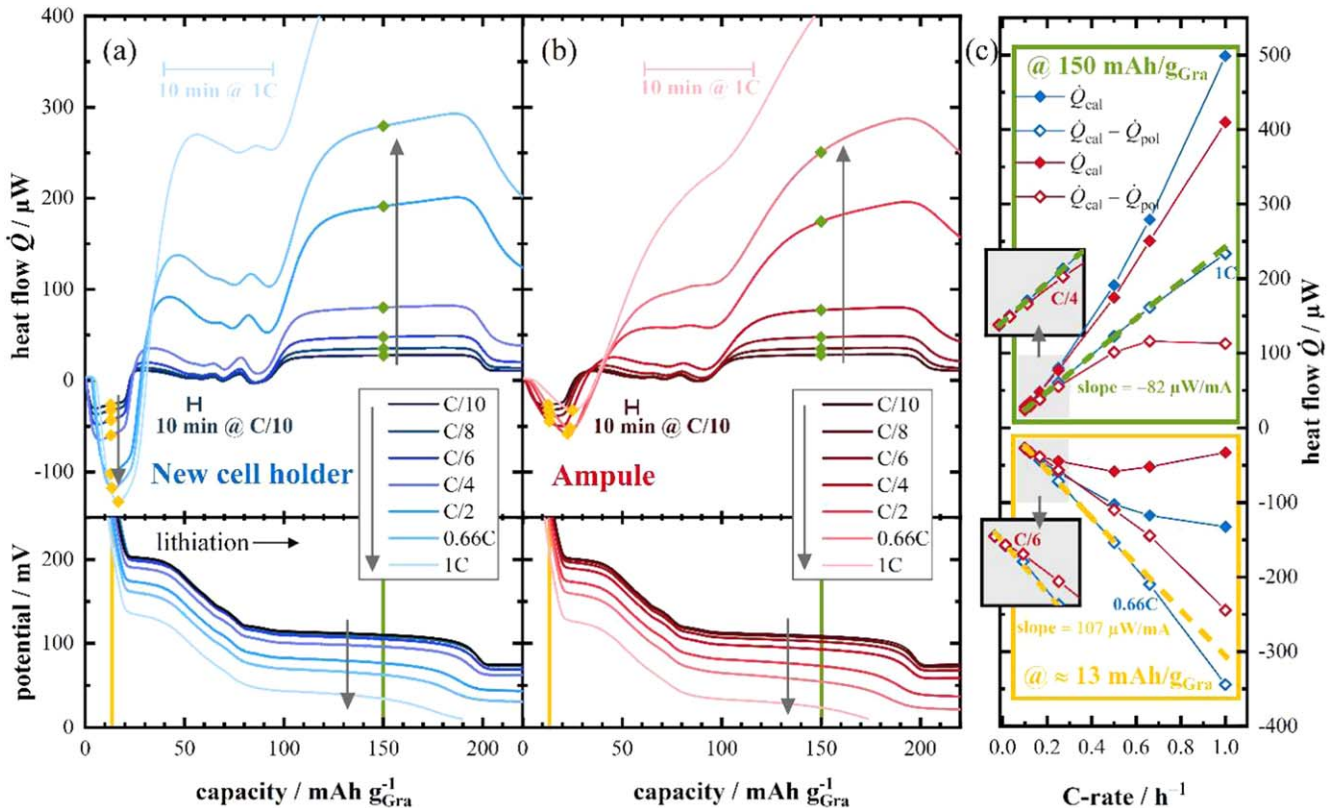


Figure 8. As-measured heat flow and cell potentials versus capacity during the lithiation of graphite in a graphite/lithium coin cell for CC cycling between 10 mV and 1.0 V. The data is plotted in the range 0–220 mAh g_{Gra}^{-1} and the cell specifications are given in the caption of Fig. 7. Heat flow and cell potential at different C-rates recorded with the new cell holder (a) and with the ampule setup (b). The evolution of features with increasing C-rate is indicated with gray arrows and the upper and lower horizontal bars represent the duration of 10 min at 1 C and C/10, respectively. (c) Analysis of the C-rate dependency of the heat flow values at 150 mAh g_{Gra}^{-1} and at ~ 13 mAh g_{Gra}^{-1} , whereby the here plotted data are indicated in panels a and b with the respective color (yellow, green). The subtracted \dot{Q}_{pol} was estimated from an analysis of overpotentials at the respective SOC and an estimated E_{eq} obtained by the mid-point line between the charge and discharge curve at C/10. Linear fits (dashed lines) were plotted for the calculated $\dot{Q}_{cal} - \dot{Q}_{pol}$ values from the new cell holder measurements for the C-rates C/10 to C/2 at ≈ 13 mAh g_{Gra}^{-1} and C/10 to 0.66 C at 150 mAh g_{Gra}^{-1} . The slopes are labeled whereby the C-rate is converted to the discharge (i.e., negative) current (C-rate*3.011 mAh). The lowest C-rates for which deviation from the linear fit is observed, are labeled for the new cell holder and the ampule (see grey region magnified in inset for lower C-rates).

(iii) parasitic heat \dot{Q}_p :

$$\dot{Q}_{cal} = \dot{Q}_{pol} + \dot{Q}_{rev} + \dot{Q}_p = I \cdot (E_{load} - E_{eq}) + \frac{I}{nF} \cdot T \cdot \Delta S + \dot{Q}_p \quad [6]$$

where I is the current, E_{load} the potential under load, E_{eq} the equilibrium potential, T the temperature, F the Faraday constant, n the number of transferred electrons per lithium (i.e., $n = 1$), and ΔS the change in entropy. As E_{load} is a function of I , \dot{Q}_{pol} scales more than linearly with the current ($\propto I^2$ for small overpotentials), whereas \dot{Q}_{rev} scales linearly. \dot{Q}_{pol} is always exothermal, while \dot{Q}_{rev} , under isothermal conditions, has equal quantities of endothermal and exothermal contributions over a full charge/discharge cycle. For the measurements with both cell holders, it can be seen that the exothermal features are shifted upwards with increasing C-rate. For the measurement in the new cell holder, the distinct endothermal peak in the range from 0–25 mAh g_{Gra}^{-1} grows with increasing C-rate (yellow markers in Figs. 8a and 8b). This indicates that in this capacity range, \dot{Q}_{rev} is dominating the overall heat flow. As most parasitic processes (e.g., SEI formation on graphite and on the lithium counter electrode) are expected to occur mostly over the first cycles, and as high coulombic efficiencies were obtained in the cycles shown in Fig. 8 (>99.8% at C/10), we assume that the contribution of \dot{Q}_p is small in comparison. On the other hand, the contributions from the polarization heat \dot{Q}_{pol} can be determined from the difference of the cell potential

E_{load} and the equilibrium potential E_{eq} (see Eq. 6), whereby the latter can be estimated as the mid-point line between the charge and the discharge curve at the slow rate of C/10.

Figure 8c shows the C-rate dependency of the as-measured heat flow \dot{Q}_{cal} (solid symbols) at two selected capacities, namely at 150 mAh g_{Gra}^{-1} (green markers in Figs. 8a and 8b) and near 13 mAh g_{Gra}^{-1} (yellow markers in Figs. 8a and 8b); for the latter, the analyzed heat flow values at higher C-rates were selected based on the feature shape in order to account for the non-negligible shift of the peak with C-rate in this region. As \dot{Q}_{pol} can be determined reasonably accurately (see above), subtracting it from the measured heat flow \dot{Q}_{cal} allows to quantify the sum of the reversible and the parasitic heat flows:

$$\dot{Q}_{cal} - \dot{Q}_{pol} = \dot{Q}_{cal} - I \cdot (E_{load} - E_{eq}) = \dot{Q}_{rev} + \dot{Q}_p \quad [7]$$

The obtained values for $\dot{Q}_{cal} - \dot{Q}_{pol}$, for the measurements with the new cell holder, appear to follow a linear trend over most C-rates (see blue open symbols in Fig. 8c). For 150 mAh g_{Gra}^{-1} an almost perfect linear fit can be obtained for the C-rates from C/10 to 0.66 C (see dashed green line), and for 13 mAh g_{Gra}^{-1} from C/10 to C/2 (see dashed yellow line). This perfectly linear current dependency suggests that \dot{Q}_{rev} is the only significant contribution to this quantity and that \dot{Q}_p must be negligible (as one would expect based after

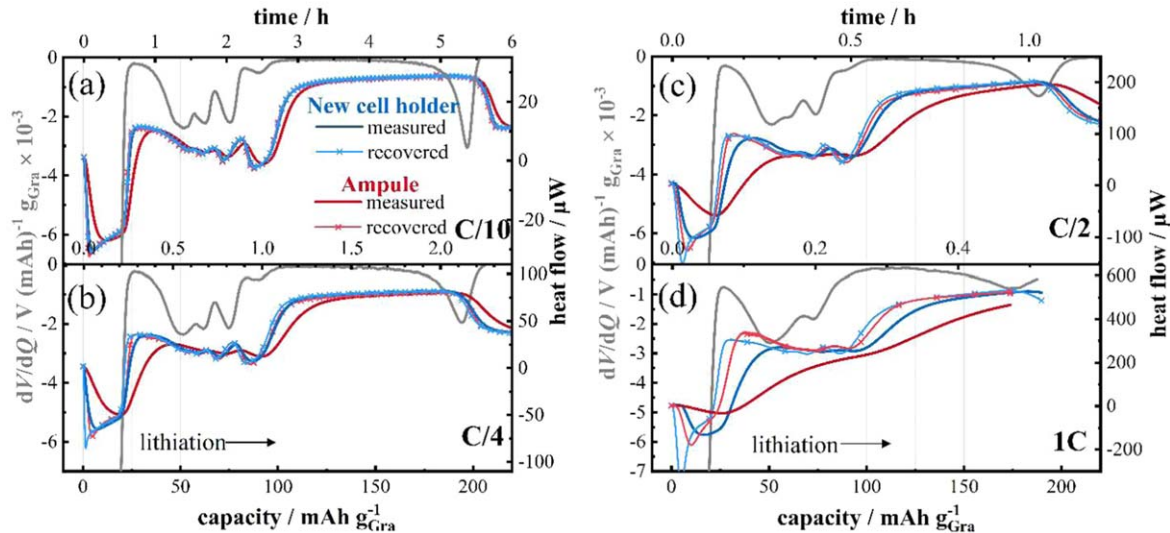


Figure 9. Measured heat flow during the lithiation of graphite in a graphite/lithium coin cell cycled between 10 mV and 1.0 V, using the new cell holder (blue) and the ampule setup (red) as well as the respective recovered heat flow signals obtained using the dynamic correction method. The differential cell potential of the cell tested in the new cell holder is plotted in gray. The cell specifications are given in the caption of Fig. 7.

extensive formation and for a coulombic efficiency of >99.8%). From the slope of the linear fit (green and yellow dashed line in Fig. 8c), an estimate of ΔS can be obtained via the following relationship:

$$\text{slope} \approx \frac{d\dot{Q}_{\text{rev}}}{dI} = \frac{T\Delta S}{nF} \quad [8]$$

For the features at 13 mAh $\text{g}_{\text{Gra}}^{-1}$ and 150 mAh $\text{g}_{\text{Gra}}^{-1}$, the values of the linear slopes marked in Fig. 8c yield ΔS values of $35 \text{ J mol}^{-1} \text{ K}^{-1}$ and $-26 \text{ J mol}^{-1} \text{ K}^{-1}$, respectively. These are similar to the values reported in the literature, which were estimated from the temperature dependency of the OCV or obtained from simulations.^{24–27} For example, Reynier et al.²⁴ and Mercer et al.²⁶ performed entropy measurements in graphite/lithium half-cells for a large number of SOCs. From interpolation between the measured data points in their reported figures (Fig. 4 in Ref. 24 and Fig. 2a in Ref. 26) entropy values at 13 mAh $\text{g}_{\text{Gra}}^{-1}$ can be roughly estimated as 38 and 45 J $\text{mol}^{-1} \text{ K}^{-1}$ and at 150 mAh $\text{g}_{\text{Gra}}^{-1}$ as -17 and $-10 \text{ J mol}^{-1} \text{ K}^{-1}$, respectively. Small differences in the measured entropy values for graphite can generally be explained by a different degree of structural ordering in the analyzed graphite material.²⁸ The current dependency of $\dot{Q}_{\text{cal}} - \dot{Q}_{\text{pol}}$ at low C-rates measured with the ampule also follows the same linear slope found for the measurements with the new cell holder. However, at increased C-rates the values deviate significantly from this behavior. This is a result of the decreased time resolution, which leads to a damping of the features at higher C-rates. In Section III we showed that the time response of the ampule measurement is a factor of 3.6 slower compared to that of the new cell holder (see Fig. 4). This suggests that a 3.6 times higher C-rate can be applied for the new cell holder before observing the damping of features. Indeed, the C-rates at which we observe the first significant deviation from the linear behavior for the ampule and new cell holder are a factor of 4.0 apart from each other. For the more dynamic feature at 13 mAh $\text{g}_{\text{Gra}}^{-1}$, we observe deviation from the linear fit at C-rates of C/6 and 0.66 C for the ampule and new cell holder, respectively (see labeled C-rates in yellow panel of Fig. 8c). At 150 mAh $\text{g}_{\text{Gra}}^{-1}$, the feature is less dynamic and, thus, the heat flow can generally be resolved at higher C-rates. The deviation from the linear fit is found at C/4 and 1 C for the two different holders (see labeled C-rates in green panel of Fig. 8c).

The dynamic correction method described above was applied to both the signal recorded in the ampule and in the new cell holder, considering the respective step-response signals characterized using the charcoal dummy cell. Figure 9 shows the as-measured and the recovered signals at selected C-rates. Since we have seen that the differential voltage coincides with the graphite heat flow features (Fig. 7), it is plotted for each C-rate to give an indication on how many distinct heat flow features are expected at the different C-rates. Even though the lithiation on the thin graphite electrode is not significantly transport-controlled, small offsets in SOC over the thickness of the electrode (i.e., more overlap of different lithiation stages) are reflected in the less distinctive features in the differential voltage curve at higher C-rates.

At C/10, both recovered signals overlap with the as-measured signals recorded in the new cell holder (Fig. 9a). This suggests that at such a low C-rate, the dynamics of the new cell holder are sufficient to resolve the graphite lithiation heat flow features as a function of SOC. It also shows that the parameters used for the dynamic correction were accurate, suggesting that the charcoal dummy cell is indeed a good model for the heat flow dynamics of the graphite/lithium half-cell. For C/4, the signal measured in the ampule is shifted quite significantly (thick solid line in Fig. 9b), but can again be corrected to match the recovered signal recorded in the new cell holder (thin blue line with symbols). Even the small features in the range from 50–90 mAh $\text{g}_{\text{Gra}}^{-1}$, which are significantly damped in the as-measured signal, can be reconstructed accurately (thin red line with symbols). When comparing the raw and recovered signal from the new cell holder, a small shift of the features to lower capacities can be observed, together with a slight enhancement of the signal amplitudes. The recovered signal shape matches that obtained for C/10 shown in Fig. 9a.

When increasing the current to C/2 (Fig. 9c), a significant loss in heat flow feature resolution can be observed for the ampule measurement. When performing the dynamic correction for these signals, the features can be remarkably well recovered. However, there remains a small offset to the recovered signal from the new cell holder. The dynamically most challenging feature in the graphite lithiation heat flow is presumably the endothermal peak at the beginning of lithiation. Here, the heat flow changes from an almost vertical decrease to an increase, thus, the heat flow signal slope changes rapidly. At higher C-rates, a greater loss of information is expected regarding such distinct features. This can lead to a damping in the recovered heat flow signal, suggesting that the absolute heat flow value at this feature must be interpreted with caution. As more

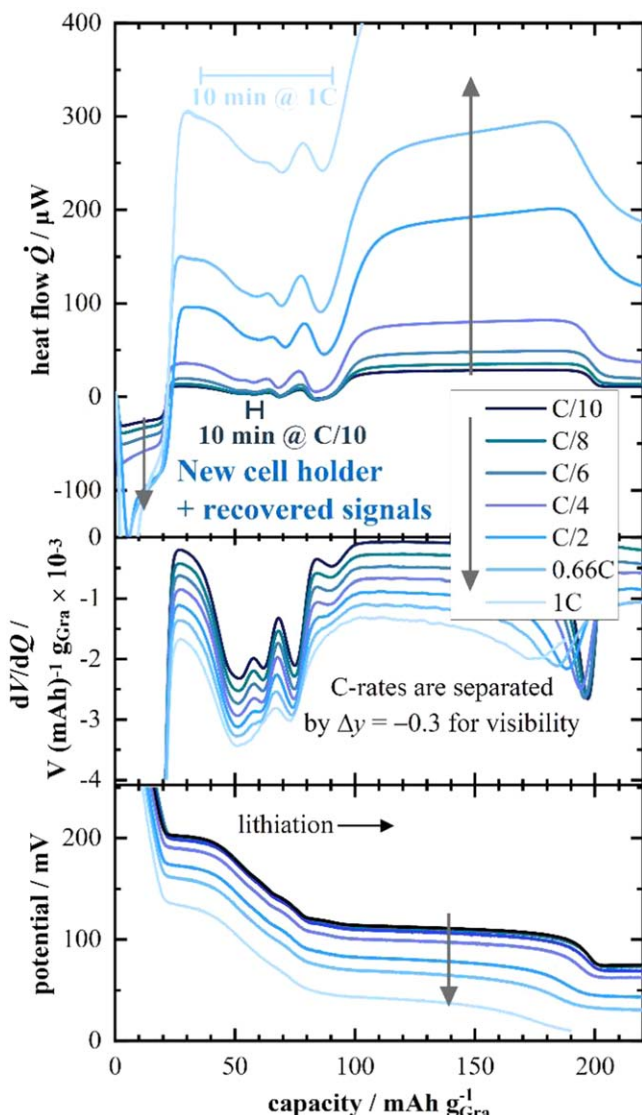


Figure 10. Graphite lithiation heat flow curves (top panel) obtained using the dynamic correction method (recovered data from Fig. 8a), recorded with a graphite/lithium half-cell cycled between 10 mV and 1.0 V (for cell specifications see the caption of Fig. 7). The evolution of features with increasing C-rate is indicated with gray arrows. The upper and lower horizontal scale bars represent the duration of 10 min at 1 C and C/10, respectively. The lower and middle panel show the lithiation potentials and their first derivatives respectively. To better distinguish the dV/dQ curves, the data are shifted by $-0.3 \text{ V} (\text{mAh})^{-1} \text{ g}_{\text{Gra}} \times 10^{-3}$ between each increasing C-rate.

dynamic information is preserved for the measurement with the new cell holder, the recovered signal is expected to be more accurate. At 1 C (Fig. 9d), the signal is also significantly damped for the new cell holder. However, the dV/dQ curve also indicates that the changes in the lithiation processes become less distinct, suggesting that this loss of features is not solely due to limitations in the time resolution of the heat flow signal. Indeed, the recovered heat flow signal displays features that closely trace those of the dV/dQ curve.

Figure 10 shows the recovered signals for all C-rates recorded with the graphite/lithium half-cell mounted with the new cell holder. Compared to the as-measured data (Fig. 8a), the features are more distinct. Even though at higher C-rates we see some damping of features, this, as discussed for Fig. 9c, correlates with the damping in dV/dQ features (middle panel of Fig. 10). However, for example, the distinct feature at $\sim 80 \text{ mAh g}_{\text{Gra}}^{-1}$ is clearly visible for all C-rates. In

general, the features seen for each C-rate align well and thus, as is expected, follow a very similar SOC dependency. This shows that the dynamic correction method based on the characterization of the step response with the charcoal dummy cell yields reasonable results and can be used for a better analysis of dynamic heat flow phenomena in lithium-ion batteries.

Conclusion and Outlook

A method was described for improving the time resolution of heat flow measurements by calorimetry, enabling the analysis of highly dynamic processes in lithium-ion batteries. For this, a TAM IV microcalorimeter was used in combination with a new coin cell holder design, which was optimized to maximize the heat transfer dynamics from the coin cell to the calorimeter. This resulted in a significantly improved resolution of the highly dynamic heat flow features observed during the lithiation of graphite in a graphite/lithium half-cell. Using a dummy cell with matched thermal properties to an actual half-cell, the time-resolution of the setup was characterized and a dynamic correction method based on the obtained parameters was presented. This enabled a quasi-SOC-resolved analysis at C-rates up to 1 C, which was demonstrated for a graphite/lithium half-cell. It was shown that the measured heat flow features appeared at the same SOC at different C-rates and that they were in excellent agreement with the features displayed by the derivative of the potential with respect to the capacity dV/dQ versus capacity curve.

Next to an analysis of features in the graphite lithiation, another possible application of highly time resolved calorimetry could be the detection and analysis of lithium-plating during fast charging. Downie et al.¹⁹ have shown that lithium plating and stripping processes exhibit distinct features in the heat flow signal. Our improved sample holder design and data post-processing method will likely enable a better analysis of such features and allow a detection of processes even when they occur over a short period of time. Furthermore, the separation of contributions to the heat flow can be done more precisely for signals with a good SOC resolution, as the current dependency is a way to identify the reversible heat flow \dot{Q}_{rev} contribution ($\propto I$). The origin of certain features in the heat flow could be better analyzed by this method and attributed to different sources of heat. For example, one could distinguish a parasitic process, which occurs at a specific SOC, from one which occurs at a specific potential. Furthermore, this method could enable a better understanding of high-energy next-generation active materials which evolve significant heat upon cycling as a result of their large voltage hysteresis (e.g., LMR-NCM, silicon).

Acknowledgments

The authors thankfully acknowledge the German Federal Ministry of Education and Research (BMBF) for its financial support within the AQua HysKaDi project (03XP0321B). We wish to thank Rüdiger Göbl and Michael Danzer for the inspiring discussion about signal processing methods and Korbinian Schmidt for the discussion about cell holder geometry. Finally, we thank Philip Rapp for the graphic illustrations of the coin cell setups.

ORCID

Alexander Kunz <https://orcid.org/0000-0003-3169-4263>

Clara Berg <https://orcid.org/0000-0002-5416-3396>

Franziska Friedrich <https://orcid.org/0000-0001-9400-1212>

Hubert A. Gasteiger <https://orcid.org/0000-0001-8199-8703>

Andreas Jossen <https://orcid.org/0000-0003-0964-1405>

References

1. X. Zhang, Z. Li, L. Luo, Y. Fan, and Z. Du, *Energy*, **238**, 121652 (2022).
2. K. Onda, T. Ohshima, M. Nakayama, K. Fukuda, and T. Araki, *J. Power Sources*, **158**, 535 (2006).

3. J. R. Croy, K. G. Gallagher, M. Balasubramanian, Z. Chen, Y. Ren, D. Kim, S.-H. Kang, D. W. Dees, and M. M. Thackeray, *J. Phys. Chem. C*, **117**, 6525 (2013).
4. D. Schreiner et al., *J. Electrochem. Soc.*, **168**, 30507 (2021).
5. L. Kraft, T. Zünd, D. Schreiner, R. Wilhelm, F. J. Günter, G. Reinhart, H. A. Gasteiger, and A. Jossen, *J. Electrochem. Soc.*, **168**, 20537 (2021).
6. T. Teufl, D. Pritzl, S. Solchenbach, H. A. Gasteiger, and M. A. Mendez, *J. Electrochem. Soc.*, **166**, A1275 (2019).
7. F. Friedrich, T. Zünd, A. Hoefling, J. Tübke, and H. A. Gasteiger, *J. Electrochem. Soc.*, **169**, 040547 (2022).
8. V. L. Chevrier, Z. Yan, S. L. Glazier, M. N. Obrovac, and L. J. Krause, *J. Electrochem. Soc.*, **168**, 30504 (2021).
9. D. J. Arnot, E. Allcorn, and K. L. Harrison, *J. Electrochem. Soc.*, **168**, 110509 (2021).
10. L. E. Downie, S. R. Hyatt, and J. R. Dahn, *J. Electrochem. Soc.*, **163**, A35 (2016).
11. L. E. Downie, S. R. Hyatt, A. T. B. Wright, and J. R. Dahn, *J. Phys. Chem. C*, **118**, 29533 (2014).
12. S. L. Glazier, S. A. Odom, A. P. Kaur, and J. R. Dahn, *J. Electrochem. Soc.*, **165**, A3449 (2018).
13. D. S. Hall, J. P. Allen, S. L. Glazier, L. D. Ellis, L. Ma, J. M. Peters, I. G. Hill, and J. R. Dahn, *J. Electrochem. Soc.*, **164**, A3445 (2017).
14. D. S. Hall, S. L. Glazier, and J. R. Dahn, *Physical chemistry chemical physics: PCCP*, **18**, 11383 (2016).
15. J. Li, H. Li, W. Stone, S. Glazier, and J. R. Dahn, *J. Electrochem. Soc.*, **165**, A626 (2018).
16. L. Ma, L. Ellis, S. L. Glazier, X. Ma, Q. Liu, J. Li, and J. R. Dahn, *J. Electrochem. Soc.*, **165**, A891 (2018).
17. L. J. Krause, L. D. Jensen, and J. R. Dahn, *J. Electrochem. Soc.*, **159**, A937 (2012).
18. L. E. Downie, K. J. Nelson, R. Petibon, V. L. Chevrier, and J. R. Dahn, *ECS Electrochem. Lett.*, **2**, A106 (2013).
19. L. E. Downie, L. J. Krause, J. C. Burns, L. D. Jensen, V. L. Chevrier, and J. R. Dahn, *J. Electrochem. Soc.*, **160**, A588 (2013).
20. F. Cverna, "ASM ready reference: thermal properties of metals." *Materials Park* (ASM International, Ohio) (2002).
21. J. F. Shackelford, Y.-H. Han, S. Kim, and S.-H. Kwon, *CRC Materials Science and Engineering Handbook* (CRC Press, Boca Raton, FL) (2016).
22. L. Keviczky, R. Bars, J. Hetthészsy, and C. Bányász, *Control Eng.* (Springer, Berlin) (2019).
23. H. Yang and J. Prakash, *J. Electrochem. Soc.*, **151**, A1222 (2004).
24. Y. Reynier, R. Yazami, and B. Fultz, *J. Power Sources*, **119–121**, 850 (2003).
25. K. E. Thomas and J. Newman, *J. Power Sources*, **119–121**, 844 (2003).
26. M. P. Mercer, M. Otero, M. Ferrer-Huerta, A. Sigal, D. E. Barraco, H. E. Hostler, and E. P. M. Leiva, *Electrochim. Acta*, **324**, 134774 (2019).
27. D. Allart, M. Montaru, and H. Gualous, *J. Electrochem. Soc.*, **165**, A380 (2018).
28. Y. F. Reynier, R. Yazami, and B. Fultz, *J. Electrochem. Soc.*, **151**, A422 (2004).